Dislocation mechanism based model for Portevin–Le Chatelier like instability in microindentation of dilute alloys

G. Ananthakrishna* and Srikanth K
Materials Research Centre, Indian Institute of Science, Bangalore 560012, India

(Received 22 March 2019; revised manuscript received 29 July 2019; published 14 August 2019)

Although the topic of intermittent plastic flow manifesting as load fluctuations or displacement jumps in nanoindentation (depths less than 100 nm) has attracted considerable attention, the existence of steps on load-indentation (F-z) curves reported in microindentation (depths of several microns) of samples of dilute alloys of varying concentrations and load dates, has received little attention from a modeling point of view. Following our earlier approaches to nanoindentation instabilities and indentation size effect, we develop a minimal dislocation mechanism based model that predicts all the generic experimental features by setting up time-evolution equations for the mobile, the forest, dislocations with solute atmosphere, and the geometrically necessary dislocation densities. The model includes basic dislocation mechanisms common to most plastic deformations, such as dislocation multiplication, storage, and recovery mechanisms. We model the indentation instability as a variant of the standard Portevin–Le Chatelier (PLC) effect seen in the constant strain rate condition by including collective pinning and unpinning of dislocations from solute atmosphere. The instability mechanism is further generalized to include concentration-dependent dislocation-solute interaction to capture both concentration dependence of the indentation instability and strengthening of alloy samples. Based on recent experimental observations that show small misorientation at small depths suggesting limited geometrically necessary dislocation density, we model the growth of the geometrically necessary dislocation density by the number of loops that can be activated under the contact area and the mean strain gradient. The equations are then coupled to the load rate equation. The model predicts all the generic experimental features, such as (a) the stepped nature of the F-z curves, (b) the existence of a critical load and critical indentation depth for the onset of the instability, (c) the decreasing dependence of the maximum indentation depth with concentration of the alloying element, (d) the mean critical indentation depth z^* for the onset of the instability increasing with decreasing concentration with a concomitant increase in levels of fluctuations, (e) the decreasing power-law dependence of the critical indentation depth with concentration, (f) the manifestation of intermittent stepped response in a window of load rates, and (g) the magnitude of the load steps scaling linearly with the load. In essence, the basic physical mechanisms responsible for predicting all the experimental results (a)–(g) are the generalization of pinning and unpinning mechanism (of dislocations from solute atmosphere) to include concentration-dependent dislocation-solute interaction and solution hardening of alloy samples with concentration together with the inherent rate-dependent nature of the PLC instability.

DOI: 10.1103/PhysRevB.100.064102

I. INTRODUCTION

The inherently intermittent motion of dislocations is now well recognized. Two types of intermittencies have been identified in the past few decades, one observed in small volume systems and another in bulk systems. Examples of the first type are seen in serrated stress-strain curves of micrometer rods when their diameter is decreased below a fraction of a micron [1]. In contrast, intermittent plastic flow also manifests in bulk samples of dilute metallic alloys when they are deformed at constant strain rate, known as the Portevin–Le Chatelier (PLC) effect [2–5]. Clearly, the underlying dislocation mechanisms in these two cases are very different.

Equivalent scenarios in indentation experiments are also known. For instance, intermittent behavior is seen in nanoindentation experiments (i.e., depths is less than 100 nm) of pure metals as load serrations in displacement controlled (DC) experiments [6] or displacement jumps in the load controlled (LC) experiments [7]. Then, the equivalent of the PLC instability in indentation of bulk samples of dilute alloys is the manifestation of steps on the F-z curve, a topic mainly pursued by two groups [8–15]. The focus of these two groups is different aspects of the instability. The Hungarian group [8–13] reports detailed study of the nature and concentration dependence of the stepped response whereas the Russian group [14,15] reports characterization of different waveforms of the stepped response by developing a high accuracy measurement technique for depth and load for a fixed concentration. The topic has received significantly less attention compared to nanoindentation instabilities [6,7]. In particular, little attention has been paid to model the phenomenon.

Detailed indentation experiments on dilute alloys of varying concentrations by Lendvai and co-workers has demonstrated that most characteristic features expected of alloys exhibiting the PLC effect, such as the negative strain rate

*Corresponding author: garani@iisc.ac.in

 ©2019 American Physical Society

sensitivity (SRS) of the flow stress are seen in these experiments [8–13]. These are as follows: (a) Steps reflective of the instability appear on the F-z curve, (b) there exists a critical indentation depth z^* for the onset of the instability, (c) the maximum indentation depth of the stepped F-z curve (for a fixed load) decreases with concentration c of the alloying element, (d) the mean critical indentation depth z^* for the onset of the instability increases with decreasing concentration with a concomitant increase in the magnitude of fluctuations, (e) the critical indentation depth z^* exhibits a decreasing power-law dependence on concentration, (f) the stepped response is seen only in a window of load rates, and (g) the magnitude of the load steps scales linearly with the load. These features are generic to several dilute alloys (such as Al-Mg and Al-Cu). The stepped F-z response translates as oscillatory hardness in the region of instability. Chinh *et al.* [13] propose a model to explain the discontinuous flow by assuming a "N" shaped hardness function to mimic the negative SRS feature of the PLC effect. Although the model captures the stepped nature of the F-z curve, *the model does not predict* other features.

Although these observations have been known for over 20 years, there is a total absence of any kind of simulations or models that predict these results. The purpose of the paper is to devise a dislocation mechanism based dynamical model along the lines of the Ananthakrishna (AK) model for the PLC effect [3,16–23], the two models of nanoindentation instabilities [24–26], and the model for indentation size effect (ISE) [27] with a view to predict all the *generic features (a)–(g)*.

Considering the fact that the stepped F-z curves is a manifestation of the PLC effect in indentation experiments, it is useful to recall the salient features and the basic instability mechanism of the PLC effect. The PLC instability manifests itself as irregular stress serrations seen in a window of strain rates $\dot{\epsilon}_a$ and temperatures [3–5]. Three types of serrations, namely, types C, B, and A, associated with static, partially, or fully propagating bands have been identified [3–5,16,17,20–23]. The physical mechanism attributed to the PLC instability is the collective pinning and unpinning of dislocations from a solute cloud. The instability arises as a competition between the waiting time of dislocations temporarily arrested at obstacles and diffusion timescale of the solute atoms, commonly called dynamic strain aging. At lower $\dot{\epsilon}_a$, there is sufficient time for solutes to diffuse to dislocations implying higher concentration at dislocation cores. Consequently, higher stress is required to unpin dislocations from the solute atmosphere resulting in large stress drops. Increasing $\dot{\epsilon}_a$ leaves less time for solutes to diffuse thereby reducing the unpinning stress and, hence, to smaller amplitude serrations. The slow pinning of dislocations and their abrupt unpinning from solute atmosphere induces negative SRS of the flow stress at macroscopic scales [3,4,16,17,19]. Indeed, most models of the PLC effect use negative SRS feature in some form [28–30].

Noting that the above experiments report a detailed study of the influence of increasing concentration, the standard PLC instability mechanism should now be generalized to include concentration dependence of pinning and unpinning of dislocations from a solute cloud. In addition, we need to devise a way to include strengthening mechanism of alloys with concentration. These two steps are essential since there are no reports of concentration-dependent experimental studies on the PLC effect. For the same reason, there has been neither theoretical attempts to model concentration dependence of pinning and unpinning of dislocations from the solute cloud (including the AK model) nor modeling the influence of alloy strengthening on the instability features [3,16,17,19,23].

Indeed, the absence of any model or simulation can be attributed to the inability to model or simulate two basic experimental features viz.: (a) concentration dependence of the stepped response and (b) the indentation process is intermittent [8–13]. Neither including concentration-dependent dislocation-solute interaction nor simulating displacement jump instability is straightforward. These points need some elaboration. As for point (a), we first recall that the underlying mechanism of the PLC effect is the same as that for steps on the F-z curve, and therefore, we can adopt the mathematical mechanism used in the AK model for explaining the salient features of the PLC effect [3,16,17,19,23]). In addition, we generalize the PLC instability mechanism to include concentration dependence of dislocation-solute interaction to account for concentration-dependent experimental features of the indentation instability. Noting that the PLC effect is a rate-dependent instability, generalization of the PLC instability mechanism is expected to automatically induce rate dependence also. As for point (b), even in the case of LC mode nanoindentation instability where a limited number of displacement jumps are seen, only one simulation attempts to predict the displacement jumps but manages to predict *only a slope change* beyond the elastic limit corresponding to the first displacement jump in experiments [31]. In contrast, our recent model for LC mode instability not only predicts all the generic experimental features, but also provides a good fit to experimental data [24–26]. The fact that there are no simulations (or models) so far to predict stepped response is related to the inherent difficulty in simulating (or modeling) jump instabilities.

The above discussion suggests that most appropriate tools to model are those that can capture jump instabilities and concentration-dependent features. Then, the nonlinear dynamical approach is the most appropriate platform for describing any instability, in particular, the displacement jumps. Similarly, since plastic flow is completely determined by dislocation mechanisms, the dislocation mechanism based approach provides a natural basis. Indeed, the AK model for the PLC effect, the two models on nanoindentation instabilities and the ISE model are all based on dislocation mechanisms. In addition, considerable information on dislocation mechanisms contributing to different types of deformation processes are well documented in the literature [32].

The proposed model includes standard dislocation mechanisms, such as dislocation multiplication, storage, and recovery mechanisms [24,25,27]. In addition, we adopt the collective pinning and unpinning mechanism of dislocations from the solute cloud from the AK model [3,16,17,19,23]. We also introduce concentration-dependent dislocation-solute interaction to account for the concentration-dependent features.

Following our earlier work [24–27], we develop time-evolution equations for the four types of (volume/sample averaged) dislocation densities, namely, the mobile ρ_m, the forest ρ_f [identified with the statistically stored

dislocations (SSD) in the standard notation], dislocations with solute atoms ρ_c, and the geometrically necessary dislocations (GNDs) ρ_G. Furthermore, following Ref. [27], we model the growth of the GND density based on the recent experimental observations [33–35] that show small misorientations at small depths suggesting limited geometrically necessary dislocation density. We also include solute diffusion to the GNDs that are embedded in the solute environment. These equations are coupled to the load rate equation. As we will show, the model predicts all the generic experimental features listed as (a)–(g) without exception. The most important conclusion emerging from this paper is that concentration dependence of pinning and unpinning of dislocations from the solute atmosphere and strengthening mechanism of alloy samples with concentration together with inherent rate dependence of the PLC instability mechanism are responsible for predicting all the experimental results (a)–(g).

II. APPROACH

The basic premise of our approach is that volume/space averaged dislocation densities are adequate to predict the time-dependent stepped response of the F-z curves. This is based on the observation that the experimental load-displacement F-z curve is also a specimen/volume averaged response arising from dislocation activity in the sample. Indeed, by itself, the F-z curve or the stress-strain curve in the PLC instability contains *no information about the heterogeneous nature* of the deformation. Furthermore, it is a well known that averages are insensitive to the nature of the distribution, a result applicable to spatial averages as well. Indeed, even though the PLC effect is a complex spatiotemporal phenomenon, the original AK model that uses volume/space averaged densities *successfully predicts several generic features*, such as the existence of the instability within a window of strain rates, the existence of critical strain for the onset of the instability, the different types of serrations found with increasing strain rate, the negative SRS feature [17,19], and the existence of chaos which has been subsequently verified [3,4,18,36,37]. Even our recent models on LC mode nanoindentation instability [25,26] and the ISE [27] not only predict all the generic experimental features, but also provide *good fits to experimental data.* (See Fig. 2(a) of Ref. [25], Fig. 7(b) of Ref. [26], and Figs. 8 and 12 of Ref. [27]). Thus, the success of these models justifies using sample/space averaged dislocation densities for describing the stepped nature of load-displacement curves.

III. BACKGROUND

The total indentation depth z measured from the undeformed $z = 0$ surface to the tip of the indenter, is the sum of the elastic z_e and plastic displacement z_p. Then, we have

$$z = z_e + z_p. \tag{1}$$

As stated in the Introduction, our approach is fully dynamical implying that all variables evolve with time in a coupled nonlinear manner. This means that z, z_e, and z_p are all dynamical variables. The elastic displacement z_e is easily determined by inverting the indenter specific load-displacement function $F = F(z_e)$. In contrast, calculating the plastic displacement z_p is not straightforward. The strength of our approach lies in calculating the plastic strain rate $\dot{\epsilon}_p$ [24] using the Orowan equation,

$$\dot{\epsilon}_p = bV(\sigma)\rho_m \tag{2}$$

to obtain z_p. Here, b is the magnitude of the Burgers vector, $V(\sigma)$ is the mean velocity of dislocations, and σ is the stress. Since our approach uses strain as the basic variable, and since plastic deformation occurs inside the sample of thickness $\mathcal{T}$, a natural strain variable is $\epsilon = z/\mathcal{T}$. Then, the total strain ϵ is given by

$$\epsilon = \frac{z}{\mathcal{T}} = \frac{z_e}{\mathcal{T}} + \frac{z_p}{\mathcal{T}} = \epsilon_e + \epsilon_p. \tag{3}$$

Then, Eq. (1) reads

$$z(t) = z_e(t) + \mathcal{T}b \int V[\sigma(t)]\rho_m(t)dt. \tag{4}$$

Note z is time dependent.

Equation (2) assumes that $\rho_m(t)$ can be calculated in some way. Furthermore, since Eq. (2) is a function of stress (σ), it should be expressed in terms of the load F and area A. The functional dependence of F and A on z are nonlinear and indenter specific. This, in turn, enables us to abstract the average stress under the indenter surface as indentation proceeds. The most general form of $F(z_e)$ is given by

$$F = CE^* z_e^q, \tag{5}$$

where q and C are constants to be determined and E^* is the effective modulus of the indenter and the sample. q ranges from 1.5 to 2 with $q = 1.5$ corresponding to a spherical indenter and $q = 2$ corresponding to a Vickers or Berkovich indenter. E^* is given by

$$\frac{1}{E^*} = \frac{1-\nu_s^2}{E_s} + \frac{1-\nu_i^2}{E_i}, \tag{6}$$

where ν and E refer to Poisson's ratio and Young's modulus of the sample and indenter, respectively. The constants C and q in Eq. (5) depend on the material and indenter geometry and, therefore, must be determined by fitting Eq. (5) to the measured elastic F-z_e curve.

Strictly speaking, contact area A is defined in the elastic region and is expressed in terms of the elastic contact depth z_{e_c}, i.e., $A = A(z_{e_c})$. Furthermore, the contact area is generally a complicated function of z since the shape of the indenter is the composite shape of the Vickers and blunted indenter. Approximate expressions have been suggested in literature that can be fitted to measures shape of the blunted indenter [38,39]. The leading contribution to A comes from the geometry of an ideal indenter. For a Vickers or Berkovich indenter, the area is given by $A(z_{e_c}) = 24.54 z_{e_c}^2$. However, real indenters are always blunted. The shape of the blunted tip determined by scanning electron microscopy or atomic force microscopy measurements [38,39] can be approximated by a sphere of nominal radius R with an area $A_H = 2\pi R z_{e_c}$. Then, the area $A(z_{e_c})$ can be approximated by

$$A(z_{e_c}) = 24.54 z_{e_c}^2 + 2\pi R z_{e_c}. \tag{7}$$

In general, the elastic depth z_e is a function of the contact depth z_{e_c}, i.e., $z_e = z_e(z_{e_c})$. Then, the measured elastic contact area when fitted with Eq. (7) determines $z_e = z_e(z_{e_c})$. Often, a linear approximation $z_{e_c} \approx s z_e$ is adequate. Although Eq. (7) is strictly valid in the elastic region, we assume that it is valid in the elastoplastic region also. This is based on the observation that during the stepped F-z response seen in the elastoplastic region, the load increases in a near-elastic manner following displacement jumps. This can only happen if the increased area (arising from bursts of plasticity) makes contact with the indenter surface. Thus, we have

$$A(z_c) = 24.54 z_c^2 + 2\pi R z_c, \tag{8}$$

in the elastoplastic region. Here, $z_c = z_{e_c} + z_{p_c}$ is the total indentation depth from the contact point, and z_{p_c} is the plastic component of z_c. We also assume $z_c = sz$ is valid.

In the LC mode of indentation, the applied load rate is held constant, i.e.,

$$\frac{d}{dt} F[z_e(t)] = \dot{F}_0 = \text{constant}. \tag{9}$$

Noting that Eq. (4) is a function of σ and, hence, a function of both F and A, it is clear from the above discussion that both the experimentally measured F-z_e curve and $A(z_{e_c})$ are crucial inputs into our model. Since both these data sets are not given, the scope of our model is limited to predicting the generic features.

Since the plastic displacement z_p should be obtained by calculating the plastic strain rate $\dot{\epsilon}_p$, the problem boils down to setting up the time-evolution equations for the four dislocation densities.

IV. DISLOCATION MECHANISMS BASED DYNAMICAL MODEL

A. General form of time-evolution equations for dislocation densities

Having identified the four types of dislocations, namely, the mobile, the forest, dislocations with a solute cloud, and the GNDs, we now consider the possible dislocation mechanisms that transform one type of dislocation to another and use them for developing time-evolution equations for the respective densities ρ_m, ρ_f, ρ_c, and ρ_G. These mechanisms can be broadly categorized into dislocation multiplication which in the present case is concentration dependent, storage and recovery mechanisms, and collective dislocation effects. Since the latter is concentration dependent, it requires inclusion of dislocation-solute interaction.

Three dislocation mechanisms determine the extent of plastic flow, namely, dislocation multiplication, storage, and recovery mechanisms. The growth of ρ_m is controlled by multiplication of initial dislocations. This is written as $\theta V_m(\sigma)\rho_m$. Here, $V_m(\sigma)$ is the average velocity of dislocations, and θ is the inverse of an appropriate length scale (see for details Refs. [3,23–25]). However, in the present context, concentration dependence needs to be included [see the expression for $V_m(\sigma)$ below]. Of the several the phenomenological expressions suggested in the literature for $V_m(\sigma)$ [40], we use a power-law expression,

$$V_m(\sigma) = V_0 \left[\frac{\sigma_{\text{eff}}}{\sigma_m(c)}\right]^m = V_0 \left[\frac{[\sigma - h(\rho_f + \rho_G)^{1/2}]}{\sigma_m(c)}\right]^m. \tag{10}$$

Here, V_0 is a reference velocity, $\sigma_m(c)$ which, in the present case, is a concentration-dependent dislocation multiplication threshold, m is the velocity exponent, $\sigma_{\text{eff}} = h(\rho_f + \rho_G)^{1/2}$ is the effective back stress, $h = \alpha G b$, G is the shear modulus, and $\alpha \sim 0.3$–0.5. Within the scope of our model, we regard the line length increase due to Frank-Read source or cross slip, etc., as dislocation multiplication processes.

To appreciate concentration dependence of dislocation multiplication threshold $\sigma_m(c)$, consider a pure metal. Recall that dislocations move in the medium of other dislocations and obstacles where they are arrested. As stress increases, dislocation segments between pinning points bow out. Then, dislocations surmount these obstacles only when the applied stress exceeds breakaway stress. Then, dislocations multiply rapidly, and hence, the breakaway stress is identified with dislocation multiplication threshold stress σ_m.

However, introducing an alloying element into a pure metal strengthens the alloy since the solute field impedes dislocation motion [41]. Two types of dislocation-solute interactions are relevant for our paper, namely: (a) One leading to an increase in the yield stress σ_y and (b) the other leading to concentration dependence of the unpinning stress of dislocations from the solute cloud. Consider the first. Generally, dislocation multiplication threshold σ_m is a lower bound of σ_y, and for all practical purposes, $\sigma_y = \sigma_m$ [3,25,27]. For solid solutions, σ_y and, hence, σ_m increase with concentration c, i.e., $\sigma_m = \sigma_m(c)$ increases. In indentation experiments [8–13], this feature is reflected in $z_{\max}$ decreasing with concentration for a given $F_{\max}$. The exact form of $\sigma_m(c)$ needs to determined.

Two types of strengthening mechanisms have been identified in the literature [41,42]; weak pinning where dislocations are pinned by isolated solute atoms and strong pinning identified with pinning by closely spaced groups of solute atoms [41]. For low concentrations, dislocations interact with isolated solute atoms. Since the number of points at which dislocations are pinned depends on solute concentration, the flow stress depends on c. Expressions for critical resolved shear stress τ_s for low c have been derived assuming that solute atoms are uniformly dispersed. Later, it has been argued that uniform dispersion is invalid except at very low c [41,42].

For higher concentrations relevant for our case, dislocation pinning and break away involves groups of solute atoms [41,42]. Then, the critical resolved shear stress is given by $\tau_s = [\frac{f_m^4 c^2 w}{E_L b^2}]^{1/3}$, where w is an interaction length scale, E_L is the line tension, and f_m is the maximum unpinning force [42]. The change in the exponent value basically arises due to statistical fluctuations in the local density of solutes that pin the dislocation line [42].

Later, a correlation has been suggested between the yield stress and the concentration of the form [43]

$$\sigma_y(c) = \sigma_y(0) + \sigma_s c^n. \tag{11}$$

Here, $\sigma_y(0)$ is the yield stress of the pure metal, and σ_s is the increase in the yield stress per (at. % of solute)^n [43]. The strengthening exponent is $n = 2/3$. Often, n is taken to range

from 0.5 to 0.75. Since σ_m is the lower bound of the yield stress σ_y, we consider $\sigma_m(c)$ follows a similar dependence on c. Thus, we have

$$\sigma_m(c) = \sigma_m(0) + \sigma_s c^n. \tag{12}$$

Here, $\sigma_m(0) = \sigma_m$ is the multiplication stress of a pure metal and, hence, known. σ_s is the stress per (at. % of solute)^n, to be determined by matching Eq. (12) with experiments.

We now consider concentration dependence of the instability mechanism underlying the stepped nature of the F-z curves, namely, pinning and unpinning of dislocations from the solute atmosphere, the same as that in the PLC effect. Following the AK model, this mechanism is mimicked by introducing dislocations with a solute cloud (with a density ρ_c) based on the physical picture that solute atoms diffuse to mobile dislocations temporarily arrested at obstacles. Then, the corresponding loss rate to ρ_m is given by $\alpha_m \rho_m$. The rate constant α_m depends on solute concentration c in the bulk, D_c is the diffusion constant of the solutes, and λ is an effective attractive length scale (see Ref. [23]). Then,

$$\alpha_m(c) = D_c(T)c/\lambda^2 = \alpha_m(0)c. \tag{13}$$

Then, the rate constant, that was originally considered as a constant (in the AK model), acquires concentration dependence. Thus, $\alpha_m(0)c\rho_m$ is the source term for the growth of ρ_c. Within the scope of the AK model, we consider those mobile dislocations that start acquiring solute atoms as dislocations with solute atoms ρ_c. As dislocations progressively acquire solute atoms, they are eventually immobilized and, therefore, grouped under immobile forest dislocations. Therefore, $\alpha_c\rho_c$ is a loss term to $\dot{\rho}_c$ with a loss rate $\alpha_c\rho_c$ [44]. This term acts as a source term to $\dot{\rho}_f$. This also means that ρ_f contains those dislocations that have acquired a solute cloud. This is in addition to the dislocation junctions that constitutes large proportion of forest dislocations.

In the AK model, dislocations immobilized by solute cloud can be reactivated. This term, represented by $\lambda_0\rho_f$, is a loss term to $\dot{\rho}_f$ and a gain term to $\dot{\rho}_m$. Then, $\lambda_0\rho_f$ represents that fraction of ρ_m which has been immobilized due to solute pinning. In this representation, the unpinning transformation is represented in terms of the *concentration-independent unpinning rate*. However, in reality, unpinning of dislocations should depend on concentration of solutes at the core of dislocations. This, in turn, depends on solute concentration in the bulk. As shown in Appendix C, concentration-dependent unpinning stress σ_c can be written as

$$\sigma_c = e_f c(t)\left(\frac{3}{4b^3}\right)\left(\frac{R_c^2}{\Delta b}\right)E_b = \sigma^* c. \tag{14}$$

where E_b is the binding energy per solute atom, e_f is the enrichment factor in the core, R_c is the radius of the solute cloud, and Δ is the distance by which the dislocation has to be pulled before it is unpinned from the solute cloud (typically $\Delta \approx 2R_c$). Clearly, σ_c depends on the nature of the metal, the alloying element, and the binding energy between the solute atoms and the dislocations. Recent studies on Al-Mg alloys using atom probe tomography show that the enrichment factor is 2.5 [45]. Using typical parameter values, $R_c = 5$ b, $\Delta = 2$, $b = 2.85$ nm, $e_f = 2$, and $E_b = 0.06$ eV, we get $\sigma_c = 20$ MPa per unit concentration. Then, the rate of dislocations unpinned from the solute cloud is given by $\lambda_0(\frac{\sigma}{\sigma_c})\rho_f$. This is a loss term for $\dot{\rho}_f$ and a gain term for $\dot{\rho}_m$.

We now consider various dislocation-dislocation interactions that transform one type of dislocation to another. As dislocations multiply, they begin to interact with other dislocations to form dipoles and junctions. Since these mechanisms have been discussed in our recent papers [25–27], we will be brief in explaining these mechanisms. Dipoles are formed when two dislocations moving in nearby glide planes approach a minimum distance (∼a few nanometers). This mechanism contributes a loss term of $\beta\rho_m^2$ to $\dot{\rho}_m$, which is a *storage* (or a source) term for $\dot{\rho}_f$. Here, β is a rate constant. A more dominant *contribution* of the form $\delta\rho_m\rho_f^{1/2}$ to $\dot{\rho}_f$ comes from the intersection of dislocations moving on different glide planes. This is a loss rate for ρ_m [3,24–27]. This is also called the forest hardening term since the resolved shear stress is large on several intersecting planes, a mechanism that begins to contribute in stage II. Therefore. larger values of δ represent higher work hardening rate $\frac{d\sigma}{d\epsilon}$. Finally, a mobile dislocation can also annihilate a forest dislocation. This produces a common loss (recovery) term $f\beta\rho_m\rho_f$ for both $\dot{\rho}_m$ and $\dot{\rho}_f$. Here, f is a dimensionless constant. Higher values of f limit plastic flow since the mechanism removes mobile dislocations which otherwise would contribute to plastic deformation.

Now, consider dislocation mechanisms contributing to the growth of the GND density. Here, we follow the physical picture adopted in the ISE model [27], which itself was based on recent experimental observations using electron backscatter diffraction (EBSD) and transmission electron microscopy (TEM) [33–35]. These experiments show only small misorientations at small depths implying low GND density [33,34]. These authors show that hardness at small depths is largely determined by limited dislocation sources activated due to small contact area. The subsequent decrease in H with z is attributed to the increase in the number of dislocations activated due to increased contact area A [27,33–35]. Thus, the number of dislocation loops of a certain size activated is proportional to A. As demonstrated in our ISE model [27], this mechanism also removes the divergent nature of hardness H for small z predicted by the Nix-Gao model [46].

Following this physical picture, we assume that mobile dislocations are captured at a rate determined by the product of the mean strain gradient and the number of loops of a certain size (to be determined) that are activated under the contact area. Thus, the growth rate for ρ_G is proportional to: (a) ρ_m, (b) the strain gradient $\tan\phi/a$, where ϕ is the angle between the indenter and the undeformed surface, and $a = \sqrt{A/\pi}$ is the contact radius, and (c) the contact area A. Note that the proportionality to A implies that the number of loops remain small at small z increasing with z. The number of loops punched out is estimated by noting that maximum stress concentration occurs at the tip of the indenter that has a nominal radius R. Then, the size of the loops punched out is determined by the contact area of a spherical indenter $A_H = \pi a_H^2 = \pi Rz$. Thus, the number of (half) loops activated under the contact area is given by $A(z)/0.5\pi Rz$. Then, the loss rate for ρ_m is given by $V_0'\rho_m A(z)\frac{\tan\phi}{a0.5\pi Rz}$. Here, V_0' is a reference velocity introduced for dimensional consistency. In principle, V_0' is different from V_0 used in Eq. (10). However, to minimize

the number of parameters, we use $V_0' = V_0$. Furthermore, the growth rate of ρ_G is equal to the loss rate for ρ_m. In addition, we assume that recovery processes can be ignored without altering the basic conclusions for the following reasons. (a) The recovery mechanism manifests only at high ρ_G, which, however, is $\leqslant 10^{14}/\mathrm{m}^2$ as we will show. (b) In our approach, hardness H is determined by the ratio of the load to the residual imprint area and not by the SSD and GND densities as in the hardness model based on the Taylor relation for the flow stress [46]. (c) Finally, ignoring recovery mechanisms helps to limit the number of parameters simplifying the model without altering the basic conclusions.

Finally, noting that since the GNDs are in the solute field, solute atoms also diffuse to the GNDs. Therefore, we include $\alpha_G(c)\rho_G$ as a loss term for $\dot{\rho}_G$. Following our earlier arguments leading to Eq. (13), we write $\alpha_G(c) = \alpha_G(0)c$. This constitutes a gain term for $\dot{\rho}_c$. Furthermore, since the GNDs cannot be made mobile even with high stress, they will be aged fully. Since we have ignored the recovery term in $\dot{\rho}_G$, for the sake of consistency, we have dropped the loss term $\alpha_G(c)\rho_G$ in $\dot{\rho}_G$.

Collecting the loss and gain terms for ρ_m, ρ_f, ρ_c, and ρ_G, the time-evolution equations can be written as [47]

$$\dot{\rho}_m = \theta V_0 \rho_m \left[\frac{\sigma - h(\rho_f+\rho_G)^{1/2}}{\sigma_m(c)}\right]^m - f\beta\rho_m\rho_f - \delta\rho_m\rho_f^{1/2} - \beta\rho_m^2 - \alpha_m(c)\rho_m + \lambda_0\frac{\sigma}{\sigma_c}\rho_f - V_0\frac{\tan\phi}{a}\frac{A(z)}{0.5\pi Rz}\rho_m, \tag{15}$$

$$\dot{\rho}_f = \beta\rho_m^2 - f\beta\rho_m\rho_f - \lambda_0\frac{\sigma}{\sigma_c}\rho_f + \delta\rho_m\rho_f^{1/2} + \alpha_c\rho_c, \tag{16}$$

$$\dot{\rho}_c = \alpha_m(c)\rho_m - \alpha_c\rho_c + \alpha_G(c)\rho_G, \tag{17}$$

$$\dot{\rho}_G = V_0\frac{\tan\phi}{a}\frac{A(z)}{0.5\pi Rz}\rho_m. \tag{18}$$

Here, $\sigma_m(c)$ is given by Eq. (12), $\alpha_m(c) = \alpha_m(0)c$, $\alpha_G(c) = \alpha_G(0)c$, and $\sigma_c = \sigma^* c$ is given by Eq. (14).

B. Model equations for the Vickers indenter

Equations (15)–(18) are functions of stress. Noting that both load F and area A evolve in time, σ should be expressed in terms of F and A. Then, using indenter specific expressions Eq. (5) for F, Eq. (8) for A, and Eqs. (12)–(14) defining concentration-dependent rate constants in Eqs. (15)–(18), the evolution equations for ρ_m, ρ_f, ρ_c, and ρ_G take the form

$$\dot{\rho}_m = \theta V_0\rho_m\left[\frac{\frac{CE^* z_{e_c}^q}{24.5(z_{e_c}+z_{p_c})^2+2\pi R(z_{e_c}+z_{p_c})} - h(\rho_f+\rho_G)^{1/2}}{\sigma_m(0)+\sigma_s c^{2/3}}\right]^m - \beta\rho_m^2 - \delta\rho_m\rho_f^{1/2} - f\beta\rho_m\rho_f - \alpha_m(c)\rho_m + \lambda_0\left[\frac{\frac{CE^* z_{e_c}^q}{24.5(z_{e_c}+z_{p_c})^2+2\pi R(z_{e_c}+z_{p_c})}}{\sigma_c}\right]\rho_f - V_0\rho_m\frac{\tan\phi[24.5(z_{e_c}+z_{p_c})^2+2\pi R(z_{e_c}+z_{p_c})]^{1/2}}{0.5\sqrt{\pi}R(z_{e_c}+z_{p_c})}, \tag{19}$$

$$\dot{\rho}_f = \beta\rho_m^2 - f\beta\rho_m\rho_f + \delta\rho_m\rho_f^{1/2} + \alpha_c\rho_c - \lambda_0\left[\frac{\frac{CE^* z_{e_c}^q}{24.5(z_{e_c}+z_{p_c})^2+2\pi R(z_{e_c}+z_{p_c})}}{\sigma_c}\right]\rho_f, \tag{20}$$

$$\dot{\rho}_c = \alpha_m(c)\rho_m - \alpha_c\rho_c + \alpha_G(c)\rho_G, \tag{21}$$

$$\dot{\rho}_G = V_0\rho_m\frac{\tan\phi\left[24.5\left(z_{e_c}+z_{p_c}\right)^2+2\pi R\left(z_{e_c}+z_{p_c}\right)\right]^{1/2}}{0.5\sqrt{\pi}R\left(z_{e_c}+z_{p_c}\right)}. \tag{22}$$

These equations are coupled to the load rate Eq. (9). Note that these equations include explicit concentration dependence of several dislocation mechanisms contributing to the instabilities that were originally constants in the AK model.

The plastic indentation depth z_p is obtained by integrating

$$\dot{z}_p = \mathcal{T}bV_0\rho_m\left[\frac{\frac{CE^* z_{e_c}^q}{24.5(z_{e_c}+z_{p_c})^2+2\pi R(z_{e_c}+z_{p_c})} - h(\rho_f+\rho_G)^{1/2}}{\sigma_m(0)+\sigma_s c^{2/3}}\right]^m. \tag{23}$$

Equations (19)–(23) and (9) constitute a set of coupled nonlinear ordinary differential equations for microindentation of dilute alloys under a constant load rate condition. Since the model equations include all relevant dislocation mechanisms, such as pinning and unpinning of dislocations from the solute cloud (as in the PLC effect) along with concentration-dependent dislocation-solute interactions and dislocation mechanisms drawn from the ISE model [27], we expect the model to predict steps on the model F-z curves and all the generic experimental features (a)–(g) [8–13].

C. Estimation of parameter values

It is clear that the solution of Eqs. (19)–(23) and (9) depend on both experimental and theoretical parameters and, therefore, the computed F-z curves. Thus, our first step is to determine the ranges of parameters for which the model F-z curves exhibit steps in a window of loading rates. This implies that Eqs. (19)–(23) and (9) should exhibit instability in a limited range of parameter values.

The model has two types of parameters, namely, experimental and theoretical. The strength of dynamical approach is that we can directly adopt experimental parameters, such as E^*, $\dot{F}_0$, R, b, $\mathcal{T}$, $\tan\phi$, and $h = \alpha Gb$ and other shape parameters defining the indenter geometry [24–27]. Therefore, these parameters can be taken to be given. However, some experimental parameters, such as the nominal radius of the blunted indenter tip, the load rate, etc., are not generally given. Then, typical values are used. In the present case, the radius of the blunted tip used is $R = 100$–1000 nm. The thickness of the sample used in our numerical paper is 150 μm (typically $10 \times z_{\max}$). (Note, however, that the choice of $\mathcal{T}$ does not affect the results since, by definition, we have $\epsilon = z/\mathcal{T}$ and, therefore, $z = \mathcal{T}\epsilon$).

Furthermore, noting that we need to express σ as the ratio of the load F to the area A, parameters (C, q) in Eq. (5) for the force and (R, s) in Eq. (8) for the area should also be determined. These parameters can *only be determined*

TABLE I. Instability domain of model parameters. The range of $f = 1$–5.

$\sigma_m(c)/E^*$	$\dot{F}_0$ (mN/s)	m	λ_0 (s^{-1})
1/600–1/100	0.01–10	8–32	10^{-8}–5×10^{-3}
α_m	δ (m/s)	α_G (s^{-1})	α_c (s^{-1})
0.1–6.0	10^{-11}–10^{-7}	10^{-9}–10^{-4}	10^{-3}–1

by fitting the measured elastic F-z_e curve and the measured area $A(z_{e_c})$ with Eqs. (5) and (8), respectively. However, both $F(z_e)$ and $A(z_e)$ are not given [8–13]. Therefore, (C, q) and (R, s) remain undermined. Since these four parameters are crucial input data for the model, it rules out the possibility of fitting a given experimental F-z curve. However, it is possible to predict the generic features of the stepped response by assuming a typical percentage of the maximum depth $z_{\max}$ as the relaxed elastic component z_{er} after unloading, for instance, $z_{er} = 10$–$15\% z_{\max}$. ($z_{er} = z_{\max} - z_{pr}$ where z_{pr} is the residual indentation depth after unloading the indenter). The exact fraction of $z_{\max}$ used for fixing C and q in Eq. (5) does not affect qualitative features. The results presented here are for $z_{er} = 15\% z_{\max}$ [48].

Now, consider theoretical parameters. The number of theoretical parameters in a dislocation mechanism based model is determined by the number of dislocation mechanisms required to model the phenomenon. Thus, the more complex the phenomenon, the more the number of dislocation mechanisms, and the more the number of parameters. The present model includes dislocation mechanisms that control the extent of plasticity (defined by σ, ϵ or F, z), such as dislocation multiplication, storage, and recovery mechanisms. Furthermore, the model incorporates the instability mechanism, namely, pinning and unpinning of dislocations from the solute atmosphere and concentration dependence of the instability mechanism by including dislocation-solute interaction to account for the solution for the hardening effect [Eq. (12)] and concentration unpinning stress [Eq. (14)]. Each of these mechanisms contribute in a specific way to the stress-strain curves or load-indentation curves. The parameters associated with dislocation multiplication [see the first term in Eq. (19)] are $\theta, V_0, \sigma_m(0), \sigma_s, m, n = 2/3$. Similarly, the parameters associated with dislocation storage and recovery mechanisms [the second, third, and fourth terms in Eq. (19)] are β, δ, and f. Parameters associated with concentration-dependent pinning and unpinning mechanisms are $\alpha_m(0)$, α_c, $\alpha_G(0)$, λ_0, and σ_c. Although the ranges of several of these parameters have already been reported in several of earlier papers [23,27], in the present case, a great deal of simplification results from the fact that we are dealing with an instability. Then, stability analysis of Eqs. (19)–(23) and (9) provides an easy way of determining the range of values of all these parameters as discussed in detail in Appendix A. (A similar calculation has been carried out in the DC controlled nanoindentation. See the Appendix of Ref. [24]). The ranges of the parameters are listed in Table I.

One important conclusion arising from the analysis presented in detail in Appendices A and B is that the ranges of these parameters actually represent different alloys, their concentration and rate dependencies. We illustrate this by considering dislocation multiplication threshold $\sigma_m(c)$, an important parameter that controls dislocation multiplication. We first note that it is well known that, even for pure metals, the range of values of the yield stress σ_y (or σ_m) takes on a range of values from $E^*/10\,000$ to $E^*/2000$. σ_y for soft metals, such as Ag, Al, and Cu, are at the lower end and hard metals, such Ti, Ni, etc., are $E/200$. For alloys, as discussed earlier, σ_m depends on the nature of the metal, alloying element, and concentration. Indeed, Eq. (12) contains dislocation multiplications stress for the pure metal $\sigma_m(0)$ and σ_s the prefactor for concentration dependence. Both $\sigma_m(0)$ and σ_s take on a range of values that define the alloy, and therefore, the range of values of $\sigma_m(c)$ represents different alloys. 4 on decimals The situation *simplifies considerably* for a given alloy, say, Al-Mg since $\sigma_m(0) = \sigma_y$ is known for Al and σ_s is easily determined by fitting Eq. (12). Similar arguments show that the ranges of several of the parameters associated with other dislocation mechanisms represent different alloys and their concentration dependence. For details we refer to Appendix A.

V. RESULTS

Equations (19)–(23) and (9) are solved using adaptive step size Runge-Kutta solver (MATLAB ODE15S) to obtain the model F-z curves. The initial conditions used for $\rho_m(0)$, $\rho_f(0)$, and $\rho_c(0)$ are $\sim 10^8$–$10^{10}/\mathrm{m}^2$ and $\rho_G(0) = 0$. Note that $\rho_G(0) = 0$ for samples with no strain gradients arising from inclusions and other defects.

As stated in the Introduction, our main goal is to predict *all the generic features (a)–(g)* [8–13]. Of all the experimental results, the plot of the mean critical onset depth of instability $z^* = \langle z^*(c) \rangle$ as a function of concentration needs a special attention since the plot shows error bars on z^* for each c value. (See Fig. 10 of Ref. [12]). Since Eqs. (19)–(23) and (9) are a set of coupled nonlinear ordinary equations, addressing such fluctuations requires devising a novel method of calculating such fluctuations. We will show that these error bars represent sample-to-sample fluctuations in c.

Experimental features (a)–(g) can be classified into three groups, namely, (i) characteristic features of the instability, (ii) concentration, and (iii) rate-dependent features of the instability. Therefore, we begin by calculating the model F-z curves by varying concentration and load rate over ranges similar to those in experiments. Recall that concentration dependence appears in several model parameters. These are $\sigma_m(c)$, $\alpha_m(c)$, $\alpha_G(c)$, and σ_c. Due to concentration dependence, these parameters are also rate dependent. However, not all parameters are independent. For instance, the recovery $f\beta$ and storage parameters δ are not independent. This can be seen as follows. Recall that for large f (for a fixed β) the common loss term $f\beta\rho_m\rho_f$ reduces the extent of plastic flow by limiting the growth rate of ρ_m which otherwise would have contributed to plastic flow. On the other hand, as already stated, the forest hardening term $\delta\rho_m\rho_f^{1/2}$ determines the rate of hardening ($\frac{d\sigma}{d\epsilon}$), and therefore, larger δ implies higher rate of hardening. This illustrates that f and δ are not independent. Furthermore, both δ and f are also material dependent.

TABLE II. Selected set of parameter values used as reference values for calibration studies of parameters on the model F-z curves.

σ_m/E^*	$\dot{F}_0$ (mN s^{-1})	R (nm)	λ_0 (s^{-1})	α_G (s^{-1})	θV_0 (s^{-1})
1/200	1	400	5×10^{-5}	5×10^{-5}	1
β (m^2/s)	δ (m/s)	f	α_c (s^{-1})	α_m (s^{-1})	m
10^{-11}	3.16×10^{-10}	1.5	0.48	2.17	20

Similar observations hold with respect to several other parameters. See Appendix A for details.

A. Influence of parameter variation on model load-displacement curves

Although stability analysis allows us to calculate the domain of parameters where stepped F-z curves are predicted (see Table I) *does not guarantee* that the generic experimental features (a)–(g) are also realized *in the entire instability domain.* Indeed, the instability range of parameters is larger than the domain where features (a)–(g) are seen. We determine this subdomain by calibrating the influence of each parameter on the model F-z curve and helps us to locate the parameter space where the model F-z curves are similar to the experimental F-z curves for different concentrations and load rates. (See the LC mode indentation model [25] and the ISE model [27] for details). This procedure also establishes the relative importance of the various dislocation mechanisms used in the model.

Following Refs. [25,27], we begin calibrating the parameters by studying their influence on the model F-z curve. In this paper, we vary one parameter keeping the rest at suitable reference values listed in Table II.

The first step is to calibrate load F in Eq. (5) by determining the values of C and q. This is performed by assuming 10% of $z_{\max}$ is the elastic component. Using $z_{\max} = 12.54$ μm and $F_{\max} = 2N$, values drawn from a typical experimental F-z curve (corresponding to 2.7 wt % Mg shown in Fig. 4 of Ref. [13]). Using these values and $q = 1.7$ in Eq. (5), we get $C = 0.146$. ($q = 1.7$ is suggested in Ref. [11]). Here, we have used $s = 1$ in $z_c = sz$ valid for no pile-up or sink-in situation due to the absence of the measured area. However, the predicted results are valid for $z_c \neq z$ expected of pile-up/sink. (See supporting comments in Ref. [49]).

Noting that $z_{\max}$ (for a given $F_{\max}$) is the sum of elastic and plastic contributions, the first check is to ensure that $z_{\max}$ and $F_{\max}$ values in the computed F-z curve match $z_{\max} = 12.54$ μm at $F_{\max} = 2N$. Indeed, the computed model F-z curve will yield $z_{\max} = 12.54$ μm for $F_{\max} = 2N$ *only for a specific value of* $\sigma_m(c)$. To check this, we have solved Eqs. (19)–(23) and (9) using $C = 0.146$ and $q = 1.7$ by varying $\sigma_m(c)$ such that the model predicts $z_{\max} = 12.54$ μm and $F_{\max} = 2N$. (Other parameters are as in Table II). This happens only when $\sigma_m(c) = 443$ MPa. In terms of E^*, $\sigma_m(c) = E^*/170$.

We now consider the influence of the two interdependent parameters $\sigma_m(c)$ and m on the model F-z curve. Recall that, in the ISE model [27], a systematic study of the influence of the parameters on the model F-z curves showed that they are sensitive only to dislocation multiplication mechanism, i.e., to σ_m and m, and insensitive to recovery, storage mechanisms (f and δ) and other instability parameters $\alpha_m(c)$, α_c, α_G, and λ_0. In the present problem, although steps over-ride the F-z curve (for parameters in Table I), we anticipate that $z_{\max}$ of the model F-z curves would also be sensitive to $\sigma_m(c)$ and m.

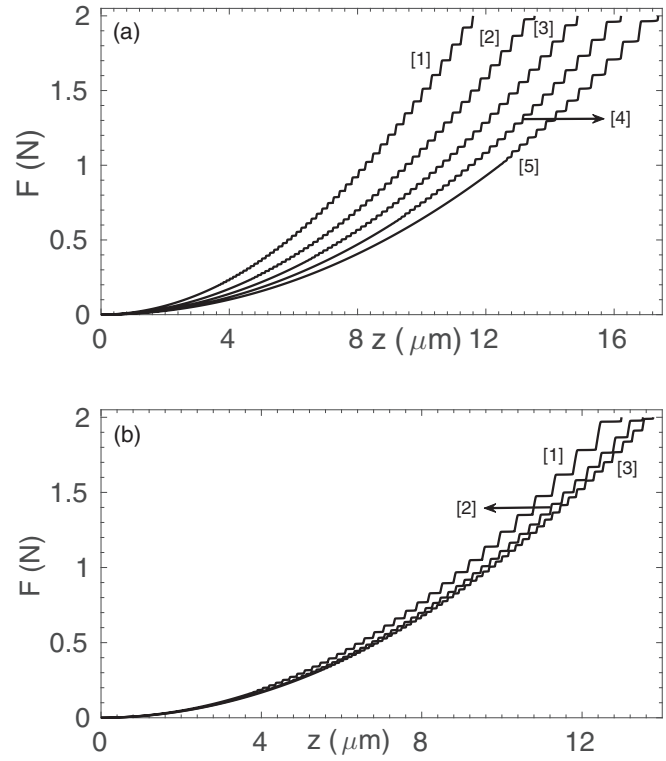

FIG. 1. (a) Model F-z curves for $\sigma_m(c) = E^*/150$ [1], $E^*/200$ [2], $E^*/250$ [3], $E^*/300$ [4], and $E^*/350$ [5] for $m = 20$. The curve [2] corresponds to the parameter values in Table II. (b) Model F-z curves for $m = 12$[1], 20[2], and 28 [3].

We first consider calibrating $\sigma_m(c)$. Since experimental results are generic features of several alloys, such as Al-Mg, Al-Cu, etc. [12], we express $\sigma_m(c)$ in terms of E^*. Then, the range of values of $\sigma_m(c)$ to be anticipated can be found by calculating stress at $F_{\max}$ and $z_{\max}$ values corresponding to the four experimental F-z plots in Fig. 8 of Ref. [12] for the Al-Mg alloys. These stress values range from $E^*/350$ for $c = 0.45$ wt % Mg to $E^*/110$ for $c = 4.5$ wt % Mg. We have varied $\sigma_m(c)$ from $E^*/110$ to $E^*/350$. Figure 1(a) shows plots of the model F-z curves for $E^*/150$, $E^*/200$, $E^*/250$, $E^*/300$, and $E^*/350$ labeled [1]–[5], respectively. Note that the F-z curve labeled [2] corresponds to parameter values listed in Table II. Therefore, curve [2] is taken as the reference model F-z curve with respect to which calibration of all parameters is carried out. Several feature are evident. All the F-z curves in Fig. 1(a) show steps as expected since the parameters are in the instability domain (Table I). Furthermore, increasing $\sigma_m(c)$ decreases $z_{\max}$. These features are consistent with the experimental F-z plots in Fig. 8 of Ref. [12]. (The decreasing $z_{\max}$ for a fixed $F_{\max}$ is predicted by the smooth F-z curves for pure metals in our ISE model. See Fig. 2 of Ref. [27]). Another feature seen from Fig. 1(a) is that the depth of onset of the steps z^* decreases with increasing $\sigma_m(c)$.

Now consider the influence of the velocity exponent m on the model F-z curve by varying m from 10 to 30. Figure 1(b) shows plots of F-z curves for $m = 12,\ 20$, and 28 labeled [1], [2], and [3], respectively. It is clear that, although increasing m increases $z_{\max}$, the change is marginal. Two other features are also clear, namely, although increasing m does not affect $z_{\max}$ much, the step size decreases with m and the onset of the instability occurs at larger depths. Furthermore, increasing the trend of $z_{\max}$ with m is opposite to the influence of $\sigma_m(c)$, a feature that was demonstrated in the ISE model also [27]. The opposite trends of $\sigma_m(c)$ and m is a direct consequence of the expression for the velocity given by $V_m = V_0[(\sigma_{\text{eff}})/\sigma_m(c)]^m$ in the dislocation multiplication mechanism that controls $z_{\max}$. Then, for fixed m, increasing σ_m decreases $[\sigma/\sigma_m(c)]^m$ and, hence, decreases $z_{\max}$, whereas increasing m for a fixed σ_m increases $z_{\max}$.

We have investigated the influence of other parameters, such as $\alpha_m(c)$, $\alpha_G(c)$, and α_c on the model F-z curve. We find that each of these parameters affects the step size marginally with very little influence on $z_{\max}$. In most cases, the F-z curves for two different parameter values almost overlap except for the step sizes. For this reason, we summarize the influence of each of these parameters without giving the relevant F-z plots.

We have studied the influence of $\alpha_m(c)$ on the model F-z curve by varying $\alpha_m(c) = 0.1$ to 6/s. Although the step size is not affected much, the onset of the instability z^* occurs for smaller depths with increasing $\alpha_m(c)$. We have varied $\alpha_G(c)$ from 10^{-8}–10^{-4}/s. At the lower end of α_G, the steps are small increasing with α_G with no effect on z^*. Similarly, we have varied α_c from 10^{-3}–1/s. The step size is large at the lower end decreasing with α_c with a concomitant decrease in z^*. Again, note that the range of these parameters represent different alloys since both diffusion constant and effective attractive length scale λ in $\alpha_m(0) = D/\lambda^2$ are alloy dependent [see Eq. (13)].

We have investigated the influence of λ_0 by varying it from 10^{-8} to 10^{-3}/s. The load steps are largest at the lower end decreasing with λ_0 with little effect on the point of instability.

We have also investigated the influence of other model parameters f and δ on the model F-z curve. Noting that the AK model [3,16,17,19,23] uses $f = 1$, we use this as a reference value and vary f from 0.1–5. The instability begins beyond $f = 0.5$. For the reference value of $f - 1$, the step size is fairly small (being close to the instability point) increasing with f. The onset point of the instability z^* also decreases with f. We have also investigated the influence of the forest hardening parameter δ on the model F-z curve by varying δ from 10^{-11} to 10^{-7} m/s. Although the step size decreases with increasing δ, the change is small. Clearly, the forest hardening parameter δ and recovery parameter f are material dependent as well.

Finally, experiments show that the instability is seen in a window of load rates. We have verified this by varying the load rate $\dot{F}_0$ over a wide range of values. Figure 2 shows F-z curves for $\dot{F}_0 = 0.175$–5 mN/s keeping other parameters as in Table II. Since these F-z curves overlap except for the differing step sizes, we have displaced successive curves by 1 μm. Clearly, the step size is the largest for the smallest rate decreasing with $\dot{F}_0$, and the instability starts at smaller z^* for smaller rates increasing with $\dot{F}_0$. These features are consistent with experiments on Al-Mg alloys (see Fig. 7 of Ref. [12]).

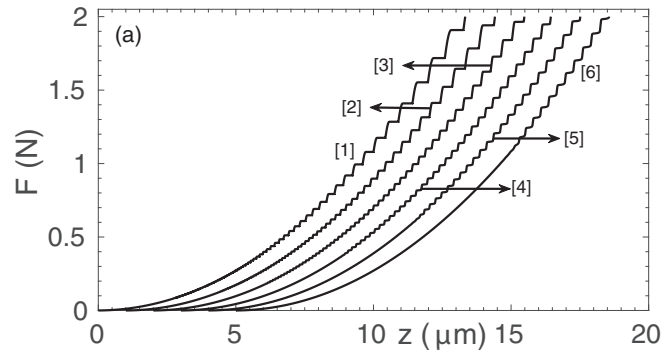

FIG. 2. Model F-z curves for $\dot{F}_0 = 0.175,\ 0.35,\ 0.7,\ 1.75,\ 3$, and 5 mN/s labeled as [1–6], respectively, each shifted by 1 μm.

Several important conclusions emerge from this paper. (i) The paper demonstrates that the model predicts steps on the model F-z curves for a wide range of values of the model parameters representing different alloys or an alloy for different concentrations and loading rates. Note that, at this point of our analysis, increasing $\sigma_m(c)$ may represent either a solution hardening of an alloy by increasing concentration or different alloys for a fixed concentration. The distinction between the two cases depends on whether $\sigma_m(0)$ and σ_s are fixed, and c is varying or whether $\sigma_m(0)$ and σ_s take on different values keeping c fixed. [See Eq. (12)]. (ii) The maximum indentation depth $z_{\max}$ of the model predicted stepped F-z curves is controlled by a dislocation multiplication mechanism since the F-z curves are sensitive only to $\sigma_m(c)$ and to a lesser extent on m. Noting that $\sigma_m(c)$ increases with c [see Eq. (12)], we see that $z_{\max}$ decreases with concentration for the given $F_{\max}$. (iii) Although dislocation mechanisms contributing to collective dislocation pinning and unpinning from the solute cloud determine the instability domain, the step size, a measure of the instability, exhibits a weak dependence on instability parameters. Since the model F-z curves are insensitive to the storage and recovery mechanisms (δ and $f\beta$) are relatively unimportant as in the ISE model [27].

VI. COMPARISON OF MODEL PREDICTED FEATURES WITH EXPERIMENTS

Since the above features (i)–(iii) of the model F-z curves are ubiquitous to a broad range of dilute alloys and load rates, we now consider calculating the model F-z curves corresponding to Al-Mg alloys used in experiments [8–13]. However, this requires that we first determine the values of $\sigma_m(0)$ and σ_s in Eq. (12) for $\sigma_m(c)$ relevant for Al-Mg alloy. As already discussed in the previous section, one easy way to do this is to use the value the yield stress σ_y to be $\sigma_m(0)$ for Al and then use Eq. (12) for various concentrations to find σ_s. However, as demonstrated by Spary *et al.* [50], σ_y [or $\sigma_m(0)$] for a pure metal is size dependent, which, for spherical indenters, manifests as larger yield stress values for the smaller indenter radius. (See Table 2 of Ref. [50]). In our case, the tip of the Vickers indenter is blunted with it effective radius R in the range of 100–1000 nm. Even for $R = 400$ nm

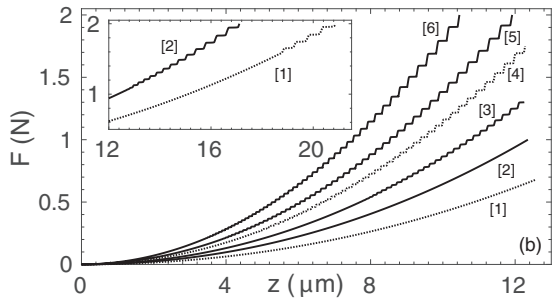

FIG. 3. Plots of model F-z curves for concentration values $c =$ 0.09, 0.45, 0.95, 1.8, 2.7, and 4.5 wt % Mg labeled [1]–[6], respectively. Note that the curves [2], [3], [5], and [6] correspond to $c = 0.45$, 0.95, 2.7, and 4.5 used in experiments. See Fig. 8 of Ref. [12]. The inset shows the onset of the instability occurring for larger depths for low concentrations $c = 0.45$ and 0.09 wt % Mg.

used in our numerical calculation (see Table II, the value of σ_y or $\sigma_m(0)$ remains undetermined.

Here, we use a self-consistent way of evaluating $\sigma_m(0)$ and σ_s. This can be performed by finding the values of $\sigma_m(c)$ for *two different concentrations* such that the model F-z curves have their $z_{\max}$ and $F_{\max}$ values matching the experimental values. Recall that we have already determined the value of $\sigma_m(c) = E/170 = 443$ MPa for $c = 2.7$ wt % Mg. Furthermore, we have also verified that the corresponding $z_{\max}$ and $F_{\max}$ of the model F-z curve match the experimental values. Then, what remains is to find $\sigma_m(c)$ for another concentration such that the model values of $z_{\max}$ and $F_{\max}$ values match the experimental values. A careful scrutiny of Fig. 1(a) shows that the F-z curve labeled [3] corresponding to $\sigma_m(c) = E^*/250 =$ 300 MPa has values of $z_{\max}$ and $F_{\max}$ close to the experimental F-z curve for $c = 0.95$ wt % Mg (see Fig. 8 of Ref. [12]). Using the values of $\sigma_m(c)$ for $c = 2.7$ and $c = 0.95$ wt % Mg in Eq. (12), we get $\sigma_m(0) = 160$ and $\sigma_s = 140$ MPa.

A. Concentration dependence of load-displacement curves

Now, we consider computing the model F-z curves as a function of concentration using Eq. (12) with $\sigma_m(0) = 160$ and $\sigma_s = 140$ MPa and then compare them with the experimental curves (Fig. 8 of Ref. [12]). Similarly, we use the linear dependence of $\alpha_m(c)$, $\alpha_G(c)$, and σ_c on concentration for computing the model F-z curves. (To compare the model F-z curves with experimental plots for various concentrations, we express c in wt % Mg).

Figure 3 shows the model $c = 0.09$, 0.45, 0.95, 1.8, 2.7, and 4.5 wt % Mg (corresponding to 0.1, 0.49, 1.05, 2.0, 3.0, and 4.97 at. % Mg) labeled [1]–[6], respectively. The concentration values $c = 0.45$, 0.95, 2.7, and 4.5 wt % Mg are chosen to facilitate comparison with the corresponding experimental curves (see Fig. 8 of Ref. [12]). Comparison shows that the model F-z curves predict the three features of experimental F-z curves (Fig. 8 of Ref. [12]), namely, decreasing $z_{\max}$ for a fixed $F_{\max}$ with increasing c or $\sigma_m(c)$, increasing step size with c and decreasing depth of onset of steps z^* with c. Even the $F_{\max}$ and $z_{\max}$ values are close to the experimental values. Even the $F_{\max}$ and $z_{\max}$ values are close to the experimental values.

Note also that the predicted F-z curve for $c =$ 0.45 wt % Mg labeled [2] remains smooth until $z_{\max} =$ 13 μm as the corresponding experimental F-z curve. However, when indentation is carried out for larger depths, we do find that the instability begins just beyond $z = 13$ μm. We have verified that the instability starts at larger indentation depths for concentrations down to $c = 0.09$ wt % Mg (or 0.1 at. % Mg). Thus, we conclude that there is no lower limit in concentration for the manifestation of the instability. Indeed, there are no reports of the existence of a minimum concentration for the onset of the PLC instability [3,5]. This result is, however, at variance with the authors' claim that there is a lower bound in concentration for the onset of the instability [12]. The authors' conclusion appears to be based on the fact that the F-z curve for the lowest concentration $c =$ 0.45 wt % Mg studied does not show any instability within $z_{\max} \leqslant 13$ μm indented (see Fig. 8 of Ref. [12]). To summarize, the predicted F-z curves for various concentrations are very similar to the experimental curves.

B. Concentration dependence of the depth of onset of the instability

Now, we consider predicting *the only experimental result that shows fluctuations*. Figure 10 of Ref. [12] shows error bars on the mean critical indentation depth $z^* = \langle z^*(c) \rangle$ for the onset of steps as a function of concentration with two distinct feature, namely, the mean $\langle z^*(c) \rangle$ increases with decreasing concentration, and concomitantly, the magnitude of the error bars also increase. However, the basic question here is: What kind of fluctuations are these? To understand this, we note that increasing fluctuations in $z^*(c)$ is similar to increasing concentration fluctuations in equilibrium statistical mechanics. Indeed, according to equilibrium statistical mechanics, concentration fluctuations are Gaussian with a standard deviation $[\langle (c' - \langle c' \rangle)^2 \rangle]^{1/2} = \sqrt{\langle c' \rangle} = \sqrt{c}$. (Here, we use c' to denote the fluctuating concentration variable to avoid any confusion. Thus, $\langle c' \rangle = c$, the mean concentration). This coupled with the fact that indentation is carried out on concentration-dependent samples suggests that the reported fluctuations in z^* are due to sample-to-sample fluctuations in concentration.

However, even predicting sample-to sample fluctuations is not straightforward since Eqs. (19)–(23) and (9) are a coupled set of nonlinear ordinary differential equations. Such equations evolve to the same state for identical initial conditions [51]. This may suggest that predicting the stochastic spread is beyond the scope of nonlinear dynamical approach. However, such equations also exhibit sensitive dependence on initial conditions. Then, our idea is to combine the inherent sample-to-sample fluctuations in concentration with sensitive dependence on initial conditions of Eqs. (19)–(23) and (9) to calculate the stochastic spread in the values of $z^*(c)$.

Sensitivity to initial conditions implies that any two trajectories corresponding to two closely separated sets of initial conditions quickly diverge in the phase space. For illustration, consider the solutions of Eqs. (19)–(23) and (9) evolved for the same time duration using two initial values of concentration c' that are close to each other, say, $c' = 3.29$ and 3.31 wt % Mg, and $\rho_m(0) = 5 \times 10^8$, $\rho_f(0) = 10^8$, $\rho_c(0) = 10^9$, $\rho_G(0) = 0(m^{-2})$ fixed. The divergence of the two

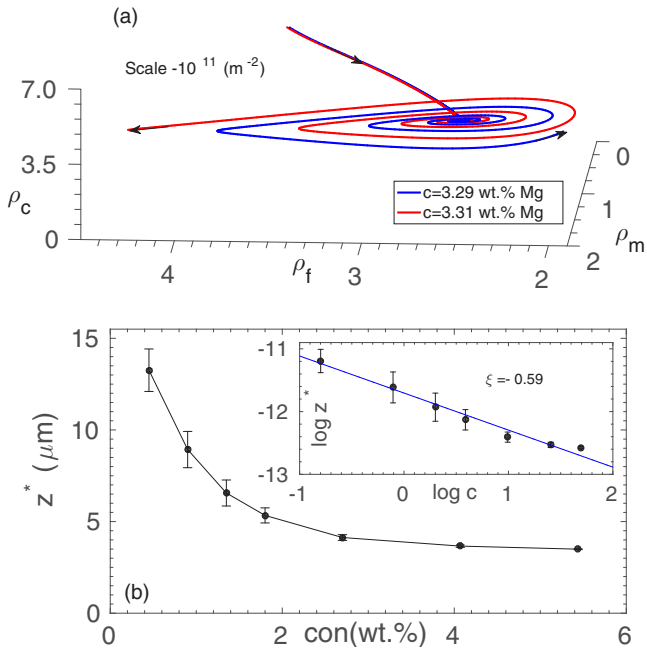

FIG. 4. (a) Phase plot obtained by solving Eqs. (19)–(23) and (9) for the same time duration using initial conditions $c = 3.2$ and 3.31 wt % Mg keeping $\rho_m(0) = 5 \times 10^8$, $\rho_f(0) = 10^8$, $\rho_c(0) = 10^9$, $\rho_G(0) = 0(m^{-2})$ fixed. Note the widely separated end points of the two orbits, a reflection of sensitive dependence on initial conditions typical of chaotic nature of the orbits. (b) A plot of the mean onset depth of instability z^* as a function of concentration along with the standard deviation. Compare Fig. 10 of Ref. [12]. The inset shows log-log plot of z^* as a function of c giving the exponent value $\xi = 0.59$.

trajectories in the phase space of ρ_m, ρ_c, and ρ_f is shown in Fig. 4(a). As is clear from Fig. 4(a), even though the two initial concentration values are very close, the trajectories quickly diverge from each other. This sensitive dependence on initial conditions also implies spread in the values of z^* even for small changes in the initial values of c'. Sample-to-sample fluctuations in concentrations are mimicked by random sampling from a Gaussian distribution with a standard deviation equal to $\sqrt{\langle c' \rangle} = \sqrt{c}$. Using c' values in this range as initial conditions, we obtain a range of $z^*(c')$ values by solving Eqs. (19)–(23) and (9).

Following this method, we have calculated both the mean $\langle z^*(c') \rangle$ and the variance $[\langle z^*(c')^2 \rangle - \langle z^*(c') \rangle^2]$ of the onset point of instability. A plot of mean $z^* = \langle z^*(c') \rangle$ along with the standard deviation $[\langle z^*(c')^2 \rangle - \langle z^*(c') \rangle^2]^{1/2}$ are shown as a function of mean concentration c in Fig. 4(b). This plot may be compared with the experimental plot for 3.3 wt % Mg concentration (see Fig. 10 of Ref. [12]). It is clear that the dependence of the calculated $z^* = \langle z^*(c') \rangle$ (•) on concentration is similar to the experimental plot. Indeed, the values of $\langle z^*(c') \rangle$ show a good fit to a power-law dependence on c of the form $\langle z^* \rangle = Bc^{-\xi}$. The inset shows a log-log plot of z^* as a function of c with $\xi = 0.59$. Note also that the exponent value of $\xi = 0.59$ is close to the solution hardening exponent value in Eq. (12).

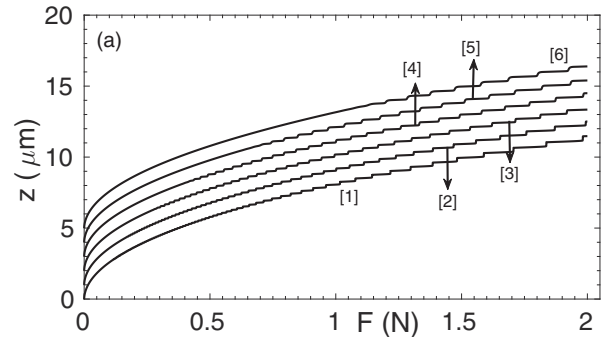

FIG. 5. Influence of the load rate on the model indentation depth—load plot for 3.3 wt % Mg or $c = 3.65$ at. % Mg. Compare Fig. 5(b) of Ref. [8]. The load rates are 0.35, 0.7, 1.75, 3.0, 6.0, and 10 mN/s labeled as [1]–[6], respectively, each shifted by 1 μm.

Sensitivity to initial conditions can also be exploited to calculate the "stochastic spread of the magnitudes and frequencies of the displacement bursts" arising from sample-to-sample fluctuations in concentration.

C. Load rate dependence of the instability

One important experimental feature is that the instability manifests in a window of load rates. Indeed, experiments carried out on Al 3 wt % Mg alloys [9,12] show that the instability is seen from 1.4 to 70 mN/s. To check this, we have varied the load rates over a wide range of values and found that the stepped response is seen in the window 0.35–10 mN/s for $c = 3.3$ wt %, a range that is slightly different from that reported in experiments. [This difference can be attributed to the assumptions made in evaluating C in Eq. (5)]. Figure 5 shows plots of model z-F curves for six different load rates labeled [1]–[6]. Note that we have plotted z-F curves instead of standard F-z curves to facilitate comparison with experimental plots (see Fig. 7 of Ref. [12]). Clearly, the step size is largest for the lowest rate decreasing with load rate. Concomitantly, the onset depth of the instability moves to larger values. It is clear that the predicted rate dependence of F-z curves is very similar to experiments.

Our detailed studies also show that the instability range of load rates is concentration dependent. For instance, the rate dependence shown in Fig. 2 for $\sigma_m(c) = E^*/200$, corresponds to $c = 1.98$ wt % Mg [using $\sigma_m(0) = 160$ and $\sigma_s = 140$ MPa for Al-Mg alloys]. Furthermore, note that the instability range is from 0.1 to 7 mN/s, a range that is different and larger than that for $c = 3.3$ wt % Mg. The concentration dependence of the instability window of load rates is physically understandable since pinning and unpinning dynamics of dislocations from the solute atmosphere depends on the imposed rate. However, this feature has not been reported in these experiments [12,13].

D. Oscillatory hardness in the instability range

Now, consider the oscillatory nature of hardness reported in experiments [12]. In our recent paper on LC mode nanoindentation instability where (limited) *displacement jumps are seen*, we demonstrated that hardness assumes two

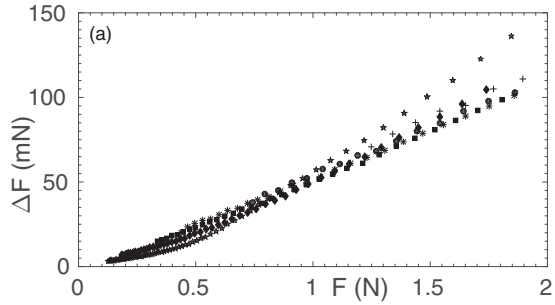

FIG. 6. Plot of ΔF versus F for concentration $c = 3.3$ wt % Mg for load rates $\dot{F}_0 = 0.35$ ($\star$), 0.7 ($\blacklozenge$), 1.75 ($\blacksquare$), 3 ($*$), 6 ($\bullet$), and 10.0(+) mN/s, respectively.

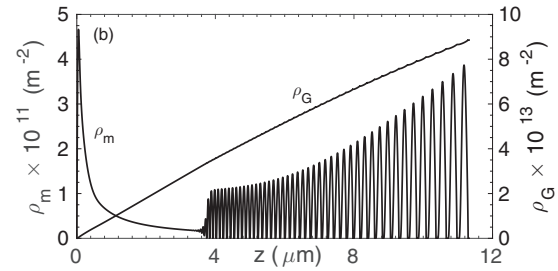

FIG. 7. Plots of ρ_m and ρ_G, respectively, as a function of z for $c = 3.3$ wt % Mg.

values [25]. It was shown that the residual indentation depth z_{pr} corresponding to the bottom and top of a load step is nearly the same. In contrast, two distinct values of z_{pr} are realized across a displacement jump. Clearly, the same argument holds for the present case where displacement jumps are seen in the instability range. Consequently, hardness fluctuates in the region of the instability.

E. Linear scaling relation between load steps and load

One characteristic feature of all the load-indentation curves (both experimental and model curves) is the increasing magnitudes of the load steps and displacement jumps with depth. Indeed, experiments show that ΔF increases linearly with F (see Fig. 9 of Ref. [8]). This features is a direct consequence of the constant load rate condition employed in indentation experiments in contrast to the constant strain rate in standard PLC experiments. Then, the corresponding effective strain rate $\dot{\epsilon}_{\text{eff}}$ is given by $\dot{\epsilon}_{\text{eff}} = \frac{\dot{F}_0}{F} \propto 1/t$ (or $\frac{\dot{z}}{z}$). This decreases with time as indentation proceeds. Noting that the stress drop magnitudes decrease with increasing strain rate in the PLC effect, the decreasing $\dot{\epsilon}_{\text{eff}}$ implies decreasing waiting time of dislocations at obstacles and, hence, increasing magnitudes of stress drops. This translates to linearly increasing magnitudes of load steps and displacement jumps with time or load. This prediction has been verified by computing ΔF as a function of F for different load rates as shown in Fig. 6. Furthermore, the fact that the slope is highest for the smallest load rate is consistent with $\dot{\epsilon}_{\text{eff}} \propto 1/t$. *These results are consistent with experiments* (see Fig. 9 of Ref. [8]). However, the plot for the lowest load rate 0.35 mN/s shows noticeable deviation from linearity for small F. This feature can be ascribed to the fact that 0.35 mN/s is close to the boundary of the instability.

F. Behavior of dislocation densities

Our approach automatically allows us to compute the four dislocation densities as a function of indentation depth or time. As in the case of the AK model, ρ_m, ρ_f, and ρ_c all exhibit oscillatory behavior. For illustration, we present a plot of ρ_m as a function of z in Fig. 7. Also shown in the same plot is ρ_G, which increases monotonically starting from a small value. This feature is in sharp contrast with the predicted divergent nature of ρ_G for z by the Nix-Gao model [46]. But this feature is consistent with the measured low misorientation (in EBSD and TEM) seen at small z or equivalently low GND density [33–35]. The monotonically increasing nature of ρ_G also suggests limited dislocation sources at small depths, a feature that is also consistent with the experimentally measured GND density (see Figs. 7 and 10 in Ref. [35]). One other feature that may be noted from Fig. 7 is the existence of tiny undulations over riding the steadily increasing ρ_G. This feature is clearly due to the fact that the growth rate of ρ_G is proportional to ρ_m, which is oscillatory.

VII. SUMMARY, DISCUSSION, AND CONCLUSIONS

The present paper is motivated by the absence of any kind of simulations or models that explain the results reported 20 years ago on microindentation of dilute metallic alloys. These studies report steps on the load-indentation curve for a range of concentrations and loading rates. The fact that neither simulating displacement jumps nor including concentration-dependent dislocation solute interaction is straightforward appears to be the reason for the absence of simulations or models.

Our approach is designed to address these features by combining the power of nonlinear dynamical methods, a natural mathematical platform for describing *the jump instability* with the dislocation mechanism based evolution equations for the four dislocation densities ρ_m, ρ_f, ρ_c, and ρ_g. The model includes two types of dislocation mechanisms. The first set includes dislocation multiplication, storage, and recovery mechanisms that are common to most plastically deforming situations. The second set accounts for dislocation pinning and unpinning from the solute atmosphere, the basic instability mechanism responsible for the stepped response. Both types of mechanisms require generalization to include concentration dependence. Three types of concentration-dependent effects are introduced to account for concentration-dependent results. First, the basic PLC instability mechanism is generalized to include concentration-dependent dislocation-solute interaction. Second, dislocation multiplication threshold stress is modified to include concentration dependence to account for solid solution hardening with concentration, and third, inclusion of concentration-dependent unpinning stress of dislocations from the solute cloud. It may be noted here that the latter two mechanisms have not been used in any PLC type of instability so far. The growth of GNDs is drawn from the hardness model for ISE [27]. To summarize, the physical mechanisms responsible for predicting all the experimental

results (a)–(g) are the generalization of pinning and unpinning mechanisms to include concentration dependence, solution hardening with concentration together with the inherent rate-dependent nature of PLC instability.

The main results and conclusions predicted by the model are summarized below. The model predicts:

(1a) Steps on the F-z curves for a range of concentrations and loading rates.

(1b) The decreasing nature of $z_{\max}$ for a given $F_{\max}$ as a function of concentration, a manifestation of solid solution hardening.

(1c) The existence of a critical indentation depth z^* for the onset of the instability.

(1d) The increasing nature of z^* and its standard deviation with decreasing concentration.

(1e) The power-law dependence of z^* on concentration with an exponent $\xi \approx 0.6$.

(1f) The existence of a stepped response in a window of (concentration-dependent) load rates.

(1g) The linear dependence of the load steps with load.

To summarize, the model predicts all experimental features without exception.

Two results deserve some comments. Recall that a novel method was devised to predict error bars on the onset point of the instability z^*c as a function of concentration as shown in Figs. 4(a) and 4(b). This has been made possible by exploiting the sensitive dependence of the set of nonlinear differential evolution equations for the four dislocation densities on initial conditions together with the inherent sample-to-sample fluctuations in concentration. This result also demonstrates the power of the nonlinear dynamical method when applied to problems in plasticity that are inherently nonlinear.

Second, since there are no PLC models that include concentration-dependent features, the theoretical basis developed here to model concentration-dependent effects can be directly adopted for modeling concentration dependence of the PLC instability. Then, the predicted results can then be used to perform experiments on a sample of varying concentrations and compare the model results with experiments.

(2) As demonstrated, since the range of the parameters physically represent different alloys and loading rates, the model predicts that the stepped response should be seen for a wide range of dilute alloys and loading rates.

(3) The steps on the F-z are sensitive *only to dislocation multiplication mechanism* determined by $\sigma_m(c)$ and to a lesser extent by the velocity exponent m and, are insensitive to storage, recovery, and other instability related mechanisms.

Finally, a major advantage of our approach is that the model equations can be solved on a desktop computer unlike simulations that require heavy computational resources, even if such simulations can be developed.

Even though our approach uses sample/volume averaged dislocation densities, our model exhibits all the experimental features (a)–(g) without exception for a range of parameter values representing different alloys, alloys of varying concentrations, and loading rates. This may come as a surprise. To appreciate this, it is important to recognize that as much as the dislocation densities are volume/sample averaged quantities, all experimentally measured quantities, such as the load, depth of indentation, residual indentation depth after unloading, etc., are also volume averages of the dislocation activity in the sample. Since both theoretically computed and experimentally measured quantities represent sample averages, the good match is not all that surprising. Moreover, it is well known that averages, including spatial averages, are quite insensitive to the details of the distribution. Viewed differently, the fact that the model predicts all experimental results without exception is clearly a validation of the mathematical tools used to describe the instability and the dislocation mechanisms used to model the physical process.

Furthermore, in the context of modeling instabilities, it is a standard practice in nonlinear dynamics to capture the time-dependent features of spatiotemporal instability *as a first step*. However, when spatial coupling appropriate to the problem is introduced, most features of spatiotemporal instability are usually captured. Indeed, the original AK model attempted only time-dependent features of the PLC instability [3,4,16–19]. (See also the Introduction). Once spatial coupling was included, the model predicted all the band types (the static type C, hopping type B, and propagating type A) [3,4,20,22,23]. It may be noted here that the heterogeneity of the three band types of bands is considerably more complex than that in indentation experiments where there is, at least, an (sectoral) angular symmetry.

From this point of view, it would be interesting to explore the possibility of using the current approach along with finite element methods to calculate the stress distribution under the indenter and then use it in our model equations to obtain spatial distribution of the dislocation activity in the sample.

ACKNOWLEDGMENTS

G.A. acknowledges the Board of Research in Nuclear Sciences Grant No. 2012/36/18-BRNS and Indian National Science Academy for a Honorary Emeritus Scientist position. We would like to thank Prof. J. Lendvai and Prof. N. Q. Chinh for clarifying several aspects relating to experiments.

APPENDIX A: ESTIMATION OF RANGES OF MODEL PARAMETERS

This Appendix is devoted to estimating the range of values of the model parameters θ, V_0, $\sigma_m(0)$, σ_s, m, $n = 2/3\beta$, δ, f, $\alpha_m(0)$, α_c, $\alpha_G(0)$, λ_0, and σ_c associated with the ten dislocation mechanisms used in the model and to determine the subdomain of parameters where stepped response is expected.

Three dislocation mechanisms determine the extent of plastic flow, namely, dislocation multiplication, storage, and recovery mechanisms, which are also material specific. Therefore, the ranges of the associated parameters represent different alloys and their concentration and rate dependencies. To see this, consider the dislocation multiplication mechanism, which is controlled by $V_m(\sigma) = V_0\{[\sigma - h(\rho_f + \rho_G)^{1/2}]/\sigma_m(c)\}^m$ given by Eq. (10). Dislocation multiplication threshold stress $\sigma_m(c)$ is taken to be the lower bound of the yield stress σ_y. This is clear from the fact that, for pure metals, σ_y (or σ_m) can range from $\sim E'/8000$ for soft metals (such as Ag, Au, and Al) to $E^*/1500$ for hard metals, such as Ni and Ti, and hence, σ_m is a material-dependent parameter.

Furthermore, since even pure metals are rate sensitive, the additional concentration dependence of alloys induces rate dependence. Thus, the range of values of $\sigma_m(c)$ represents different alloys and their rate dependencies.

For dilute alloys (Al-Mg, Al-Cu, etc.), the extent of strengthening depends on the nature of the pure metal, the alloying element, and its concentration [43,52]. Indeed, $\sigma_m(c)$ given by $\sigma_m(c) = \sigma_m(0) + \sigma_s c^n$ depends on the dislocation multiplication stress for the pure metal $\sigma_m(0)$, and σ_s is the stress prefactor for concentration dependence. For alloys used in experiments, $\sigma_m(c)$ is in the range of $\sim E^*/800$–$E^*/100$ GPa. Thus, the range of values of $\sigma_m(c)$ represent different alloys and their concentration dependences.

Now, consider other parameters in the dislocation multiplication mechanism, namely, θV_0, and the velocity exponent m. θV_0 constitutes a timescale, which, in our approach, is set to unity (1 s) to match the experimental timescale [3,4,23,25,27]. θ has an inverse dimension of length. Such a length scale in plasticity is usually taken to be the mean separation between dislocations given by $\theta \sim \rho_f^{-1/2}$. In the present case, ρ_f is typically 10^{12}–$10^{14}/\text{m}^2$ and $\theta \sim 10^6$–10^7m. Thus, $V_0 \sim 10^{-6}$–10^{-7} m/s.

In the velocity of dislocations $V(\sigma)$, both single and groups of dislocations have been measured for several metals, such as Cu, Al, Ag, and Zn and a few alloys, such as Cu-Al, Cu-Ge, etc. (see Fig. 19 of Ref. [40]). The measured mean velocity of dislocations fits the power-law expression given by Eq. (10) [40]. For pure metals (such as Cu, Al), m is close to unity, whereas it is typically $\sim$20 for the reported alloys. In addition, m also depends on the nature of metal and the alloying element as is clear from different values of m for different alloys. Therefore, m can vary considerably. Thus, m is taken to be in the range of $m = 12$–30.

Now, consider the parameters β, f, and δ associated with storage and recovery mechanisms. A standard way of estimating the allowed values of these rate constants has been discussed in a number of our earlier papers [3,19,23–25,27]. Noting that the extent of plasticity is controlled by the relative strengths of dislocation multiplication, storage, and recovery mechanisms, the values of β, f, and δ are essentially determined by the asymptotic values of ρ_m and ρ_f. Noting that Eq. (22) for ρ_G is decoupled from Eqs. (19)–(21) (due to the absence of a gain term for ρ_G), we may drop last term in Eq. (19). Then, assuming steady (asymptotic) values of ρ_m, ρ_f, and ρ_c, it is easy to show that $\beta \sim 1/\rho_m$, $f\beta \sim 1/\rho_f$, and $\delta \sim 1/\sqrt{\rho}_f$. The magnitudes of the dislocation densities also depend on the nature of the material, history of the sample, and the loading conditions. Assuming $\rho_f \sim 10^{12}$–$10^{13}/\text{m}^2$ and $\rho_m \sim 10^{11}$–$10^{12}/\text{m}^2$, we get $\beta = 10^{-11}$–10^{-12} m^2/s and $f\beta = 10^{-11}$ and $\delta \sim 10^{-9}$–10^{-6} m/s [3,4,23,25,27]. As for the range of f, we use the range of values where the instability manifest itself, which has been shown to be $f = 0.5$–5 (see Appendix B).

Now, consider the rate parameters $\alpha_m(c)$, $\alpha_G(c)$, and α_c. Of these, α_m and α_c are used in the AK model [3,16,17,20,21,23]. However, concentration dependence of α_m was not considered. From Eq. (13), $\alpha_m(c) = \frac{D_c}{\lambda^2} c = \alpha_m(0)c$ [23]. Note that $\alpha_m(0)$ is a material-dependent parameter since both the diffusion constant D_c and the effective attractive length scale λ depend on the alloy. Following our earlier work, we take $\alpha_m(c)$ to vary from 0.1 to 6.

A similar linear concentration dependence holds for $\alpha_G(c)$ also, i.e., $\alpha_G(c) = \frac{D_c}{\lambda^2} c = \alpha_G(0)c$. However, since solutes diffuse to GNDs in regions of strain gradients, D_c and λ can be significantly different. This effect is similar to the diffusion of solutes in the presence of elastic strain gradients that goes by the name of *Gorsky relaxation* for small interstitial atoms, such as hydrogen [53]. In the absence of any quantitative information, we have taken α_G to be in the range of 10^{-8}–10^{-3}/s, which is the region of instability.

As for α_c, the range of α_c was shown to be 10^{-4}–1/s for the AK model [3,16,17,20,21,23]. We use the same range here also. As for the reactivation timescale λ_0, again borrowing from our earlier work, we take the range to be 10^{-8}–10^{-3}/s [23].

One important conclusion emerging from the above discussion is that the ranges of the parameters physically represent different alloys and different loading rates.

APPENDIX B: INSTABILITY DOMAIN OF PARAMETER VALUES

A standard approach to determine the instability domain of parameters is to carry out a stability analysis of the relevant equations, here, Eqs. (19)–(23) and (9). In the present case, this is not straightforward as in the case of the AK model since the indentation is carried out under a constant load rate condition unlike the AK model where the constant strain rate condition is valid. (Note that, in the constant strain rate, loading a steady-state condition is reached and stability analysis is carried out in the steady state). In the present case, $\dot{\epsilon}_{\text{eff}} = \frac{\frac{dF}{dt}}{F} \sim 1/t$ (or, equivalently, $\dot{\epsilon}_{\text{eff}} = \frac{\frac{dz}{dt}}{z}$), which decreases as indentation proceeds. Thus, the steady state is never reached. Therefore, the stability analysis needs to be carried out at each point along the F-z curve. This turns out to be an involved exercise even numerically.

An alternate and simpler way to find the instability domain is to sweep the parameters in the physically allowed range of values. This, however, presumes prior knowledge of the approximate instability domain. Fortunately, since most dislocation mechanisms contributing to the PLC instability are drawn from the AK model, we are guided by the instability domain of the AK model. (A note of caution. The inclusion of dislocation mechanisms related to GNDs [27] can alter the instability domain). We have swept the parameters in a broad range of values around the instability domain of the AK model. The domain of instability of parameters is listed in Table I. Note the wide range of values for each of the parameters listed.

APPENDIX C: STRESS-DEPENDENT UNPINNING OF DISLOCATIONS FROM THE SOLUTE ATMOSPHERE

In general, a solute cloud formed around the core of dislocations will depend on the concentration in the bulk. Therefore, the stress required to unpin dislocations depends on concentration. This needs to be included since concentration-

dependent unpinning is not included in the AK model [3,16,17,23].

In the AK model, the pinning and unpinning processes are accomplished as a two-step transformation process with rate constants that are independent of concentration. As dislocations progressively acquire solute atoms, they are eventually immobilized at which point they are considered as immobile and, therefore, grouped with immobile forest dislocations. Therefore, the loss rate for $\dot{\rho}_c$ is $\alpha_c \rho_c$. This term is the source term for $\dot{\rho}_f$ Then, these dislocations with the solute cloud can be reactivated. This is represented by $\lambda_0 \rho_f$ with a concentration-independent rate constant λ_0. In reality, the unpinning rate should be the function of concentration-dependent stress. We, therefore, replace $\lambda_0 \rho_f$ by $\lambda_0 \frac{\sigma}{\sigma_c} \rho_f$, where σ_c is the critical stress required for unpinning dislocations from the solute atmosphere. Thus, our first job is to derive an approximate expression for the concentration-dependent unpinning stress.

Consider a straight dislocation of length l. Let N_c be the maximum number of sites in a cylindrical core of radius R_c of the dislocation for solute atoms to aggregate. This is given by $N_c = \frac{\pi R_c^2 l}{V_c}$, where $V_c = (\frac{4\pi b^3}{3})$ is the volume of a solute atom. Similarly, let the maximum number of sites available in an equivalent cylinder in bulk be N_b. Noting that the concentration of solutes in the core of dislocations is always higher than in the bulk, we may write the number of solute atoms in the cylindrical core of the dislocation $n_c = e_f n_b$, where n_b is the number of atoms in an equivalent cylinder in the bulk and e_f is the enrichment factor in the core. Then, $n_c = e_f c N_c$ and $n_b = c N_b$. The total binding energy of n_c solute atoms is $E_t = e_f c(t) N_c E_b$, where E_b is the binding energy per solute atom. Equating E_t with the work performed to unpin a straight dislocation of length l with a solute cloud of radius R_c, we have

$$\sigma b l \Delta = e_f c(t) N_c E_b, \tag{C1}$$

where Δ is the displacement that must be accomplished to unpin the dislocation from the solute cloud. The unpinning distance is typically $\Delta = q R_c$ with $q \sim 2$. Using the expression for N_c, we get the unpinning stress,

$$\sigma_c = e_f c(t) \left(\frac{3}{4b^3}\right) \left(\frac{R_c^2}{b\Delta}\right) E_b. \tag{C2}$$

Clearly, σ_c depends on the nature of the metal, the alloying element, and the binding energy between solute atoms and dislocations. Although this expression is approximate, the linear dependence of σ_c on concentration is consistent with Ref. [54]. Recent studies on Al-Mg alloys using atom probe tomography show that the enrichment factor is 2.5 [45]. Using typical parameter values of $R_c = 5b$, $\Delta = 2R_c$, $b = 2.85$ nm, $e_f = 2$, and $E_b = 0.06$ eV, we get $\sigma_c = 20$ MPa per unit concentration. (Note that we use concentration in atomic percent. However, while comparing with Al-Mg alloys, we convert it to weight percent).

Then, the fraction of ρ_f unpinned from the solute atmosphere (representing the release of mobile dislocations from the solute cloud) is given by $\lambda_0(\sigma/\sigma_c)\rho_f$. This is a loss term for $\dot{\rho}_f$ and a gain term for $\dot{\rho}_m$.

[1] M. D. Uchic, P. M. Shade, and D. M. Dimiduk, Annu. Rev. Mater. Res. **39**, 361 (2009).

[2] A. Portevin and F. Le Chatelier, C. R. Acad. Sci. (Paris) **176**, 507 (1923); A. Le Chatelier, Rev. Met. Paris **6**, 914 (1909).

[3] G. Ananthakrishna, Current theoretical approaches to collective behavior of dislocations, Phys. Rep. **440**, 113 (2007).

[4] G. Ananthakrishna, in *Dislocations in Solids*, edited by F. R. N. Nabarro and M. S. Duesbery (North-Holland, Amsterdam, 2007), Vol. 13, p. 101.

[5] A. Yilmaz, The Portevin-Le Chatelier effect: a review of experimental findings, Sci. Technol. Adv. Mater. **12**, 063001 (2011).

[6] J. D. Kiely, R. Q. Hwang, and J. E. Houston, Phys. Rev. Lett. **81**, 4424 (1998).

[7] A. Gouldstone, H. J. Koh, K. Y. Zeng, A. E. Giannakopoulos, and S. Suresh, Acta Mater. **48**, 2277 (2000).

[8] G. Bérces, N. Q. Chinh, A. Juhász, and J. Lendvai, Acta Mater. **46**, 2029 (1998).

[9] G. Bérces, N. Q. Chinh, A. Juhász, and J. Lendvai, J. Mater. Res. **13**, 1411 (1998).

[10] Z. Kovács, N. Q. Chinh, and J. Lendvai, J. Mater. Res. **16**, 1171 (2001).

[11] N. Q. Chinh, G. Horváth, Z. Kovács, and J. Lendvai, Mater. Sci. Eng., A **324**, 219 (2002).

[12] N. Q. Chinh, J. Gubicza, Z. Kovács, and J. Lendvai, J. Mater. Res. **19**, 31 (2004).

[13] N. Q. Chinh, G. Horváth, Z. Kovács, A. Juhász, Gy. Bérces, and J. Lendvai, Mater. Sci. Eng., A **409**, 100 (2005).

[14] Y. I. Golovin, V. I. Ivolgin, and M. A. Lebyodkin, Phys. Solid State **44**, 1310 (2002).

[15] Y. I. Golovin, V. I. Ivolgin, M. A. Lebyodkin, and D. A. Sergunin, Phys. Solid State **46**, 1671 (2004).

[16] G. Ananthakrishna and D. Sahoo, J. Phys. D: Appl. Phys. **14**, 2081 (1981).

[17] G. Ananthakrishna and M. C. Valsakumar, J. Phys. D: Appl. Phys. **15**, L171 (1982).

[18] G. Ananthakrishna and M. C. Valsakumar, Phys. Lett. A **95**, 69 (1983).

[19] S. Rajesh and G. Ananthakrishna, Phys. Rev. E **61**, 3664 (2000).

[20] M. S. Bharathi and G. Ananthakrishna, Phys. Rev. E **67**, 065104(R) (2003).

[21] M. S. Bharathi, S. Rajesh, and G. Ananthakrishna, Scr. Mater. **48**, 1355 (2003).

[22] G. Ananthakrishna and M. S. Bharathi, Phys. Rev. E **70**, 026111 (2004).

[23] R. Sarmah and G. Ananthakrishna, Acta Mater. **91**, 192 (2015).

[24] G. Ananthakrishna, R. Katti, and Srikanth K., Phys. Rev. B **90**, 094104 (2014).

[25] Srikanth K and G. Ananthakrishna, Phys. Rev. B **95**, 014107 (2017).

[26] G. Ananthakrishna and Srikanth K, Crystals **8**, 200 (2018).

[27] G. Ananthakrishna and Srikanth K, Phys. Rev. B **97**, 104103 (2018).

[28] P. Penning, Acta Metall. **20**, 1169 (1972).

[29] P. Hähner, A. Ziegenbein, E. Rizzi, and H. Neuhäuser, Phys. Rev. B **65**, 134109 (2002).

[30] S. Kok, M. S. Bharathi, A. J. Beaudoin, G. Ananthakrishna, C. Fressengeas, L. P. Kubin, and M. Lebyodkin, Acta Mater. **51**, 3651 (2003).

[31] M. Fivel, C. J. Robertson, G. Connova, and L. Boulanger, Acta. Mater. **46**, 6183 (1998).

[32] L. P. Kubin, *Dislocations, Mesoscale Simulations and Plastic Flow* (Clarendon, Oxford, 2012).

[33] M. Rester, C. Motz, and R. Pippan, Scr. Mater. **59**, 742 (2008).

[34] M. Rester, C. Motz, and R. Pippan, J. Mater. Res. **24**, 647 (2009).

[35] E. Demir, D. Raabe, N. Zaafarani, and S. Zaefferer, Acta Mater. **57**, 559 (2009).

[36] S. J. Noronha, G. Ananthakrishna, L. Quaouire, C. Fressengeas, and L. P. Kubin, Int. J. Bifurcation Chaos **2577**, 7 (1997).

[37] G. Ananthakrishna, S. J. Noronha, C. Fressengeas, and L. P. Kubin, Phys. Rev. E **60**, 5455 (1999).

[38] W. C. Oliver and G. M. Pharr, J. Mater. Res. **19**, 3 (2004).

[39] N. A. Sakharova, J. V. Fernandes, J. M. Antunes, and M. C. Oliveira, Int. J. Solids Struct. **46**, 1095 (2009).

[40] H. Neuhäusser, in *Dislocations in Solids*, edited by F. R. N. Nabarro (North-Holland, Amsterdam, 1983), Vol. 6, p. 319.

[41] P. Haasen, in *Physical Metallurgy*, edited by R. W. Cahn and P. Haasen (Elsevier, North Holland, Amsterdam, 1996), Chap. 22.

[42] R. Labusch, Phys. Status Solidi **41**, 659 (1970).

[43] O. Ryen *et al.*, Metall. Mater. Trans. A **37**, 1999 (2006).

[44] An integral representation of ρ_c is a lot more transparent than the verbal description. One can define $\rho_c = \alpha_m \int_{-\infty}^{t} \rho_m(t') \exp -\alpha_c(t-t')dt'$. Here, we have used a single timescale α_c for the slowing down of dislocation. Differentiating this expression leads to $\dot{\rho}_c = \alpha_m \rho_m - \alpha_c \rho_c$. The same as Eq. (21).

[45] H. Aboulfadl, J. Deges, P. Choi, and D. Raabe, Acta Mater. **86**, 34 (2015).

[46] W. D. Nix and H. Gao, J. Mech. Phys. Solids **46**, 411 (1998).

[47] In principle, we should include an equation for the solute atoms c_{core} at the core of dislocations. This is given by $\dot{c}_{\text{core}} = \alpha_c \rho_c - \alpha_m(0) c \rho_m - \alpha_G(0) c \rho_G$. The full set of equations can be easily solved but at the cost of complicating the model equations and, hence, not considered here.

[48] Unlike the present problem, both the F-z_e curve and the experimentally measured area were given for the two hardness data. This information was used to fit the predicted hardness in our ISE model [27].

[49] A simple argument is adequate to show that pile-up or sink-in situations tend to shift the multiplication threshold $\sigma_m(c)$ to smaller or larger values, respectively. To see this, consider $\sigma/\sigma_m(c) = F(z_e)/\sigma_m(c)A(z_c)$. Noting that the contact area is larger for the pile-up case compared to the ideal case, $\sigma_m(c)$ corresponding to the pile-up case should be smaller than the ideal case for the same load. The opposite holds for the sink-in case. This amounts to just a change in the $\sigma_m(c)$ value and, hence, the conclusion. Furthermore, since the range of $\sigma_m(c)$ is large, the changed values remain inside the range of values of $\sigma_m(c)$, the predicted generic features for the no pile-up or sink-in case remain unaffected.

[50] I. J. Spary, A. J. Bushby, and N. M. Jennett, Philos. Mag. **86**, 5581 (2006).

[51] S. H. Strogatz, *Nonlinear Dynamics and Chaos: With Applications to Physics, Biology, Chemistry, and Engineering* (Westview Press, Boulder, CO, 2001).

[52] R. A. Ayres, Metall. Trans. A **10**, 41 (1979).

[53] A. S. Nowick and B. S. Berry, *Anelastic Relaxation in Crystalline Solids*, Materials Science Series (Academic, New York, 1972).

[54] W. A. Curtin, D. L. Olmsted, and L. G. Hector, Jr., Nature Mater. **5**, 875 (2006).